Abstract

Title of Thesis: SIZE MODIFICATION AND COATING OF TITANIUM DIOXIDE USING A PREMIXED HYDROGEN/AIR FLAME

Seungchan Lee, Master of Science, 2006

Thesis directed by: Dr. Sheryl H. Ehrman.
Department of Chemical Engineering.

A study was conducted of the effect of flame processing on the size distribution of titania nanoparticles, and a flame process was developed for producing TiO_2/SiO_2 core-shell particles from aqueous suspensions of TiO_2 and SiO_2 nanoparticles. Both were performed using a premixed hydrogen/air flame. At the adiabatic flame temperature of 2400 K, the number mean diameter of titania primary particle increased considerably from an initial value of 44 nm to 96 nm, presumably by atomic diffusion, and viscous flow coalescence. Moreover, the majority of product particles from this high flame temperature were smooth and spherical. Based on the results of size modification experiments, coating experiments were performed. The dominant morphology observed in the product particles from coating experiments was silica coated titania. The silica

coating was very smooth and dense. The total particle size and the shell volume of the product particles were in reasonable agreement with values predicted from the atomized droplet size distribution and the droplet concentration.

SIZE MODIFICATION AND COATING OF TITANIUM DIOXIDE USING A PREMIXED HYDROGEN/AIR FLAME

by

Seungchan Lee

Thesis submitted to the Faculty of the Graduate School of the
University of Maryland, College Park in partial fulfillment
of the requirements for the degree of
Master of Science
2006

Advisory Committee:

Professor Sheryl H. Ehrman, Chair / Advisor
Professor Michael R. Zachariah
Professor Mikhail Anisimov
Professor Srinivasa R. Raghavan

Acknowledgements

I am deeply grateful for the meticulous guidance and true encouragement of my academic advisor, Dr. Sheryl H. Ehrman. I also would like to thank Dr. Michael R. Zachariah, who is my co-advisor. He, who has extensive knowledge in various areas and a passion for research, always has been a paragon to me.

Korea Science and Engineering Foundation (KOSEF), an affiliated organization of the Ministry of Science and Technology, had given financial support from September, 2004 to May, 2006. I am very thankful for their unconditional financial aid.

Finally, many thanks to members of my research group and Dr. Zachariah's research group, particularly Ranjan Pati, Sunmin Kin, and Kyle Sullivan; my friends; my family, my father Jongsun Lee, my mother Chaewha Moon, and my sister Hyojung Lee.

Table of Contents

List of Tables

List of Figures

1. Introduction

1.1 Overview of Thesis

Titanium dioxide is the most widely used white pigment because it has a higher refractive index than any other white pigment, 2.9 and 2.49 for the rutile and anatase phases respectively. For comparison, the refractive index of lead white, which is toxic, is 2.07, and the refractive index of zinc white is 2.0. Titanium dioxide also has good chemical stability, and it improves the brightness of colored pigments; appropriately sized TiO_2 particles provide more light scattering (Thiele et al., 1998).

The annual global production of titanium dioxide is around 4 million tons and of this 51 % is used as a white pigment in paints, 19 % in plastic, 17 % in paper, and 13% in a wide range of smaller applications. The consumption of TiO_2 as a pigment has increased in the last few years in textiles, food, leather, pharmaceuticals, and various titanate pigments (Carp et al., 2004).

Titanium white is attractive in sunscreen applications because of its high refractive index and optical properties of absorption and scattering of UV light (Nussbaumer et al., 2003). Titania embedded in a polymer matrix is of great interest in manufacture of UV filters, coatings to protect materials from UV, and lenses (Winkler, 2002). Titania is, however, also photocatalytically active when exposed to UV light. Surface treatment of the titania particles is essential to prevent degradation of the organic substrates by the filler titania particles.

Titania pigment particles are typically coated to control the chemical reactivity of the pigment and to protect against photocatalysis from UV radiation (Santacesaria et al., 1982a; Santacesaria et al., 1982b; Kubota et al., 2001). Silica coating on titania has been

the focus of numerous studies since Iler described the method of producing dense silica layers (Iler, 1959) because silica coating of titania yields maximum powder durability. It is, however, accompanied by loss of opacity when it is manufactured with liquid-phase method because of product particle agglomeration (Kinniard et al., 2003).

In this thesis, a new method for coating of titania particle with silica in the gas phase was investigated. Titania particles were coated by spray pyrolysis which integrates the atomization, drying, sintering, and collecting stages of core-shell system synthesis into a single continuous step. Figure 1.1.1 shows a 2-D schematic of producing silica coated titania particles in this work:

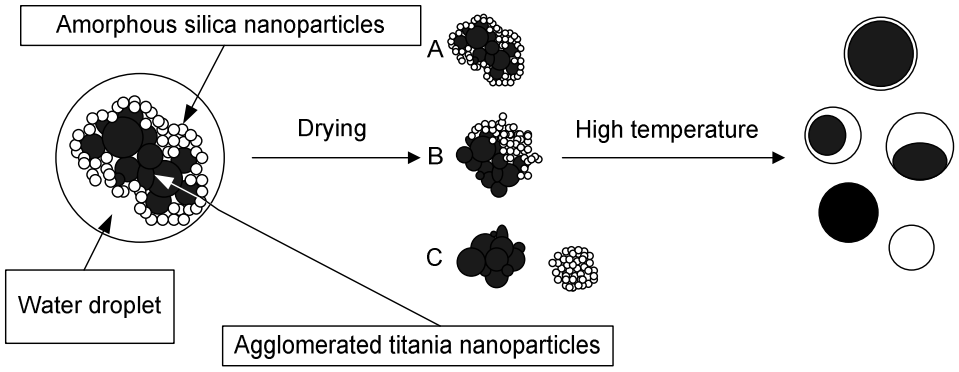

Figure 1.1.1: Schematic illustration of the process of making TiO_2/SiO_2 core-shell particles.

As starting materials, titanium dioxide nanopowders and silicon dioxide colloidal solutions were used. By employing those nanoparticles, not gas phase precursors, it was possible to focus only on sintering process of nanoparticles. A premixed hydrogen/air flame was used as a source of high temperature because it is very clean; it does not

include a hydrocarbon component in it so production of unwanted carbon containing product can be prevented. This flame provides a fairly high flame temperature, with an adiabatic flame temperature of 2400 K at stoichiometric conditions.

The remainder of this chapter consists of a literature review of the following topics: particle size and light scattering, photoactivity of TiO_2 nanoparticles, and synthesis of core-shell systems. In the second chapter, flow conditions of gases, hydrogen/air flame condition, and experimental procedure (also in appendix C) of this work are presented. Chapter Three contains a theoretical discussion about sintering rates of oxide particles and their residence time in the flame and post-flame zone. Chapter Four contains results and discussion of this thesis. In the first part of this chapter, the flame temperature effect on titania particle size modification is discussed. Silica coated titania particles are characterized with a high resolution transmission electron microscopy regarding to SiO_2 shell volume versus total product particle diameter, product particle morphology of product particles at the second part of this chapter. In Chapter Four and Five, conclusions of this thesis and recommendations for future work are presented.

1.2 Background

Photoactivity of TiO_2 Nanoparticles

All the photo-induced processes of TiO_2 initiate from the semiconductor band gap (energy gap). The irradiation of semiconducting oxides with light of greater energy than that of the band gap, 3.2 eV, leads to the formation of an exited electron in the conduction band and a vacancy in the valence band, known as a hole or h^+ (Carp et al., 2004). This excited electron can be used directly to generate electricity in photovoltaic solar cells (Fujishima et al., 2000) or to initiate a chemical reaction, which is called photocatalysis (Gratzel, 2001), or it can be scavenged by atmospheric oxygen and the photogenerated holes can lead to the generation of highly oxidizing hydroxyl radicals (HO·) that can initiate the photocatalysed degradation of the surrounding organic substrates (e.g. polymers, coatings) on the surface (DiPasquale et al., 1996; Hollande et al., 1997).

The ability to control photocatalytic activity is important in many other applications including the use of TiO_2 pigments in paint and cosmetics. A low photoactivity is required for these applications, in order to prevent chalking. This occurs during the weathering of commercial polymers and coatings containing white pigments such as TiO_2, when oxidation occurs at the surface layers of the material which eventually wears away, leaving the pigment particles exposed (Kaempf et al., 1974). Another concern is that UVC light (wavelength of 100 to 290 nm) can induce pyrimide dimer formation via photocatalysis and this molecule can damage the DNA in cells (Kubota et al., 2001).

In paint pigment applications, titanium dioxide affects the durability of paint films in two opposing ways; (a) as a strong UV absorber, TiO_2 protects the paint film, (b) as a

UV-activated oxidation catalyst, TiO_2 degrades binders. The protective role of TiO_2 has not received much attention because it is not important for the binders that are used in durable paints. The destructive effect of TiO_2, chalking, has been the subject of extensive study. A model of the chalking mechanism has been developed and verified through scanning microscopy by Kaempf et al. (Kaempf et al., 1974). They have explained the characteristics of weathered paint films in terms of binder and pigment combinations. During degradation, paint films lose mass while pigment concentration near the surface increases significantly.

The chemistry of chalking has been outlined by Volz et al. (Volz et al., 1980) who demonstrated that UV light, water and oxygen are essential to the TiO_2 catalyzed degradation of binder. They suggested the following overall reactions:

$$H_2O + O_2 + h\nu \xrightarrow{TiO_2} OH\cdot + HO_2\cdot \qquad (1)$$

Hydroxyl and peroxy radicals activate, oxidize and degrade the binder:

$$3HO\cdot + 3HO_2\cdot + 2(\text{-}CH_2\text{-}) \longrightarrow 2CO_2 + 5H_2O \qquad (2)$$

The chain of chalking events is cyclical with respect to TiO_2 and can be disrupted at the TiO_2 surface by exclusion of UV light, water or oxygen.

The encapsulation of titania pigment particles in silica can prevent contact between the catalytic surface of TiO_2 and the organic substrates and provide a surface for the recombination of free radicals. Alternatively, chalking control can be achieved by recombining holes and electrons at the TiO_2 surface via semiconductor mechanisms and hindering the reaction of the chalking cycle.

Particle Size and Light Scattering

The most important value of TiO_2 as a white pigment in the paint film is its ability to scatter visible light from a polymeric matrix effectively because this affects the opacity and tinting strength of pigment. The light scattering ability of a material is generally governed by refractive index, particle size distribution, TiO_2 content and dispersion in the polymer (Murphy, 1996). Regarding the particle size distribution, the particle size of TiO_2 pigment has been optimized experimentally and confirmed by Mie theory. The optimal size depends on the wavelength of light. For white pigment application, size is optimized for green light (wave length of 492 nm ~ 577 nm) where the human eye is most responsive. A rutile (refractive index of 2.90) sphere of 0.2 μm is optimal. As the particle size increases, the ability of the particle to scatter light increases up to a maximum at the size of 0.2 μm, then starts to decrease (Thiele et al., 1998). Mie calculations can give an optimal diameter for the scattering of an electromagnetic wave by a dielectric particle with great precision but the result is limited to the case of a single sphere. Particle crowding weakens light scattering power. A simple physical model that explains the effects of pigment particle crowding on light scattering has been suggested by Fitzwater and Hook (Fitzwater et al., 1985). They consider the loss of scattering to be caused by the overlap of optical cross-sections which are considerably larger than geometric cross-sections for pigment-size particles.

Synthesis of Core-Shell Systems

Titania pigment particles are coated to prevent contact between the catalytic surface of TiO_2 and the organic substrates and to provide a surface for the recombination of free radicals (Werner, 1969).

The conventional liquid-phase methods require several additional processes, such as immersion of the powders into the solution, coating, separation from the solution, washing, and drying. These extra processing steps significantly increase production and pollution control costs. Moreover, the coatings from liquid-phase routes are often porous leading to high oil absorption. In this thesis, titania particles were coated while they were suspended in a flowing gas with a dense silica layer by using a high temperature, gas-phase route. This continuous high temperature process has the advantage of a considerably shorter process chain compared to liquid-phase synthesis one and it leads to dense coating (Powell et al., 1996).

2. Experimental

2.1 Overview

A homemade, collision type atomizer was used to generate water droplets, with volume average diameter of 1.05 μm. As a reactor, a premixed flame burner was used to alter the size distribution of pure TiO_2 particles and to manufacture TiO_2/SiO_2 core-shell structure particles. A cone-shaped flame was selected as a flame configuration because it provides high flame temperatures, adiabatic flame temperature of about 2400 K (above the melting temperature of titania, and silica). A disadvantage of the cone-shaped flame is that because of the flame geometry, the temperature profile in the post-flame zone is not radially uniform (Glassman, 1996). The non-uniform residence time of oxide particles in the post-flame region can cause a variation in particle size and particle morphology. TEM/HRTEM was used for the product particle analysis.

2.2 Experimental Procedure

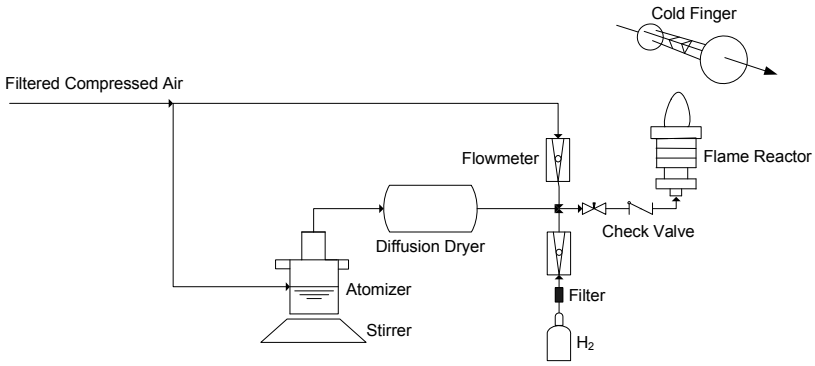

Figure 2.2.1: Schematic illustration of the experimental apparatus.

Size distribution modification and coating of titania experiments were performed in a flame reactor. Figure 2.2.1 shows a schematic illustration of the experimental

apparatus. 6 g/l TiO_2 colloidal solutions suspended in deionized water were prepared for the TiO_2 size modification experiments. The same experimental apparatus and procedure were used with the following TiO_2 and SiO_2 core-shell system construction experiment. Three different flame conditions, adiabatic flame temperature of 1800 K, 2000 K, and 2400 K, were used for the size modification experiments. Gas flow conditions for each flame temperature are shown in Table 2.2.1. Initial titanium (IV) oxide nanopowders (TiO_2 99.9 %, mixture of anatase and rutile, Aldrich Inc.) used for this experiment were originally agglomerated and the mean diameter of the particles was 44 nm (see Figure 4.1.1).

Three solutions with varying silica and titania concentration were prepared for the coating of titania experiments as given in Table 2.2.2, (a) solution of 7.5 g/l TiO_2 and 4.5 g/l SiO_2 suspended in deionized water, (b) solution of 7.5 g/l TiO_2 and 22.5 g/l SiO_2 suspended in deionized water, and (c) solution of 7.5 g/l TiO_2 and 45 g/l SiO_2 suspended in deionized water. The solution were made by mixing commercially available titanium (IV) oxide nanopowder (TiO_2 99.9 %, mixture of anatase and rutile phase, Aldrich Inc.) and silicon (IV) oxide colloidal dispersion (SiO_2, 30 % in H_2O by weight, Alfa Aesar) with deionized water. The mean diameter of the SiO_2 particles was 10 nm. To investigate the effect of salt concentration on the layer thickness, three samples were examined which were produced with solution conditions of (a), (b), and (c) at the adiabatic flame temperature of 2300 K (see Table 2.3.2). To disperse SiO_2 and TiO_2 particles in solution, the solutions were sonicated for 30 minutes prior to every experiment. The colloidal dispersion was nebulized in air with a homemade impact-type atomizer to generate aerosol droplets with a volume mean diameter of 1.05 μm. A description of how the

volume mean diameter of the droplets was determined is given in Appendix A. The solution was continuously stirred with a magnetic stir bar and stirrer during the experiments to prevent the settling of particles. The air stream was then passed through a diffusion dryer filled with silica gel to remove most of water in the droplets and the aerosol was delivered to a flame reactor along with hydrogen (98 % purity, Airgas Inc.) and an additional filtered compressed house air stream. The three different streams were combined right before the burner to create the premixed flame. The shortest possible length of Tygon tubing was used for the aerosol droplet-laden air stream to minimize the deposition of particles onto the tubing wall.

Table 2.2.1: Experimental conditions of TiO_2 size modification experiments. The flow rates are presented at standard pressure and temperature of 0 ˚C.

Adiabatic flame temperature (K)	1800	2000	2400
Hydrogen flow (LPM)	4.3	6.1	9.2
Droplet-laden air flow (LPM)	2.8	2.8	2.3
Pure air flow (LPM)	18	20	20

The flow rates of the gases at standard pressure and temperature of 0 ˚C are given in Table 2.2.2. The flow rate of the droplet-laden air stream was fixed to the maximum value possible to minimize residence time and deposition in the lines leading to the gas mixing point. To determine the flow rate of this stream, measurements were made of the flow rate leaving the nebulizer as a function of the nebulizer input pressure. The flow of hydrogen gas and additional air were controlled by rotameters which have high resolution valves and the rotameters were calibrated with an airflow calibrator (Gilibrator, Scientific Instrument Services Inc.).

Table 2.2.2: The flame and solution conditions of coating of TiO_2 experiments. The flow rates are presented at standard pressure and temperature of 0 ˚C.

Adiabatic flame temperature (K)	2300	Mass ratio (SiO_2:TiO_2)
Hydrogen flow (LPM)	8.8	
Droplet-laden air flow (LPM)	2.3	
Pure air flow (LPM)	20	
Loading of SiO_2 and TiO_2 in 80 ml water (g)	SiO_2 : 0.36, TiO_2 : 0.6	0.6:1
	SiO_2 : 1.8, TiO_2 : 0.6	3:1
	SiO_2 : 3.6, TiO_2 : 0.6	6:1

After opening the valves of the hydrogen gas cylinder and filtered compressed house air, a few minutes were required before the floating balls of flowmeters were stabilized. Although a check valve was installed prior to the flame reactor to prevent backflow of the flame to the hydrogen gas source, the flow rate of hydrogen gas was kept

lower than the set point at the beginning of the experiment to generate a stable H_2/Air flame. The flow rate of each gas was then adjusted to obtain flow rates corresponding to an adiabatic flame temperature of 2300 K.

To collect the product particles, a cold finger was used. It was positioned over the burner at a height of 15 cm from the top of the flame front and configured to have the maximum collecting area by making one of the three corners point at exactly the top of the flame front (see Figure 2.2.2). The cold finger was wrapped with a thin aluminum foil which has a collecting area of 120 cm^2 and the temperature of cooling water which passed through the three separate pipes of the cold finger was 21 ˚C. Since the stabilization of gas stream in the tubing took time whenever the valves of the rotameters were adjusted to obtain the target flame temperature to the set point, the cold finger was not moved to the collecting position until the floating balls of both rotameters were settled down and the flame was stabilized. The operating time of the flame reactor for every experiment was 2 hours.

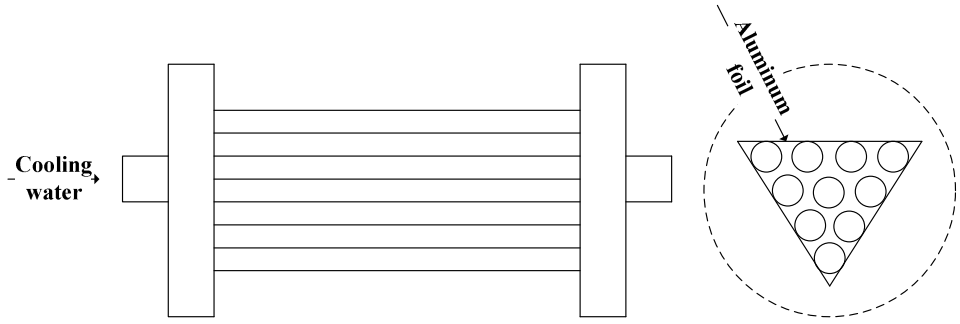

Figure 2.2.2: Cold finger configuration.

Since the product particles adhered strongly to the aluminum foil, an additional process was necessary to transfer the particles from the aluminum foil to transmission electron microscope (TEM) grids (formvar coated 200 mesh copper, Spi Supplies) for

TEM (Hitachi 600AB 100 KV) image analysis. The particles were scraped off the foil using a flat metal spatula after dropping a few droplets of filtered deionized water on the foil. The TEM grid was then directly immersed in the water suspension of product particles to collect the particles on the TEM grid.

3. Theoretical Considerations

3.1 Residence Time

In this section, the residence time of nanoparticles in the high temperature zone is calculated. Normally, a reaction zone in which the temperature is the highest refers to the actual flame region in combustion. In this thesis, however, the reaction zone includes post-flame zone which is from the flame front to the cold finger because the temperature of the post-flame zone is still high enough to cause particle sintering (see Appendix B). The effects of Brownian diffusion of particles in a boundary layer around the cold finger and thermophoretic force on product particles were not considered to the calculations of residence time in post-flame zone. It is, however, expected that the residence time in the post-flame zone is likely increased by the Brownian diffusion of the product particles in the boundary layer and decreased by thermophoresis.

Table 3.1.1 shows Reynolds numbers of gas flow in the tube for each flame condition. The flow velocity was calculated by dividing the volumetric flow rate by the orifice area of the flame reactor. All the Reynolds numbers fell into the turbulent region.

Table 3.1.1: Reynolds number of gas flow in the tube at each flame condition.

The flow rates are presented at standard pressure and 0 ˚C temperature.

Adiabatic flame temperature (K)	1800	2000	2200	2300	2400
Flow velocity (m/s)	5.2	6.4	6.6	6.7	6.8
Reynolds number	3600	4200	4300	4300	4300

The reaction time in the flame zone, τ, is related to the flame velocity through following equation:

$$\tau = \frac{\alpha}{S^2} \tag{3.1.1}$$

where α is the thermal diffusivity and S is flame velocity. The premixed flame speeds are given from the previous flow velocity calculation. Using values of thermal diffusivity evaluated at the mean of the ambient temperature (298 K) and the flame temperature, the reaction time in the flame zone was computed.

To calculate the residence time in the post-flame zone, it was assumed that the velocity is only a function of distance from the nozzle and constant with the orifice radius (Brodkey et al., 1975). From the continuity equation, the mass flow rate exiting the nozzle, w_j, can be related to the mass flow rate of downstream, w_n:

$$w_j U_j = w_n U_n \tag{3.1.2}$$

where U_j is the velocity of downstream and U_n is the velocity exiting the nozzle. The mass flow rate can be expressed by volumetric flow rate and the density of gas. The radius of the jet downstream is given by:

$$r_j = r_n + x\tan\theta \tag{3.1.3}$$

where r_j is the radius of the jet downstream, r_n is the radius of the nozzle, x is the distance from the nozzle, and θ is the angle of spread, 14 degrees. Finally, the velocity downstream can be expressed by following equation:

$$U_j = U_n \left(\frac{\rho_n}{\rho_j}\right)^{\frac{1}{2}} \frac{r_n}{r_n + x\tan\theta} \tag{3.1.4}$$

where ρ_n, ρ_j are the densities of gas at the nozzle and downstream respectively. The residence time of the particles in the post-flame zone, τ_p, can be computed by

$$\tau_p = \int_0^x \frac{dx}{U_j} \tag{3.1.5}$$

The residence time in the post-flame zone was calculated by integrating equation 3.1.5 from x = 0.025 m to 0.155 m and the values are displayed in Table 3.1.2.

Table 3.1.2: Calculation of residence time in the flame and post-flame zone.

Adiabatic flame temperature (K)	1800	2000	2200	2300	2400
Thermal diffusivity (m^2/s)	0.004 ± 0.0002	0.005 ± 0.0002	0.007 ± 0.0004	0.009 ± 0.0004	0.01 ± 0.001
Residence time in flame reaction zone (second)	0.0001	0.0001	0.0002	0.0002	0.0003
Residence time from flame front to cold finger (second)	0.025	0.020	0.020	0.020	0.019
Total residence time (second)	0.025	0.020	0.020	0.020	0.019

3.2 Sintering Rate

Koch and Friedlander (Koch et al., 1990) extended the general dynamic equation (GDE) for aerosol dynamics to include particle coalescence and sintering processes in addition to the classical collision and nucleation phenomena. They applied the extended theory, making certain approximations:

1. Formation of condensable matter is fast compared with particle formation process.
2. Sufficient time for particle growth to be independent of the initial burst of homogeneous nucleation.
3. No condensable material after homogeneous nucleation.
4. Gas flow is one-dimensional.
5. Surface free energy is isotropic and temperature independent.
6. Chemical potential gradients and atom or molecule mobilities for volume and grain boundary diffusion are identical, and mobility is isotropic.
7. Physical and thermodynamic properties of particles are those of the bulk materials.
8. The solid state diffusion coefficient is independent of pressure.

to predict primary particle size in the case of a linear cooling rate (Wu et al., 1993). For the growth of primary particles by coalescence, the final primary particle size for single component systems can be estimated using their simplified equation:

$$\frac{da}{dt} = -\frac{1}{\tau_f}(a - a_s) \tag{3.2.1}$$

where a is the surface area of the coalescing particles, a_s is the surface area of a single spherical particle of the same volume, and τ_f is the characteristic coalescence time.

Friedlander and Wu (Friedlander et al., 1994) derived a characteristic coalescence time, which can be applied to the estimation of the sintering time of titania, for the case of solid state diffusion based on a solution to the diffusion equation inside the particle, with a boundary condition relating the curvature and difference in pressure across the surface:

$$\tau_f = \frac{3kT}{64\pi v_0 D\sigma} v \tag{3.2.2}$$

Here, v is the volume of the coalescing particles, v_0 is the molecular volume for diffusion, σ is the surface tension (assumed constant), and D is the solid state diffusion coefficient. The coalescence time is controlled by the apparent diffusion coefficient of the slowest moving ion through the metal oxide. The diffusion coefficient is strongly dependent on temperature through an Arrhenius expression:

$$D = D_0 \exp(-\frac{E_a}{kT}) \tag{3.2.3}$$

where D_0 is the pre-exponential constant, E_a is the activation energy, k is the Boltzmann constant and T is the temperature.

For silica, which is assumed to sinter by a viscous flow procedure, the characteristic coalescence time is given by:

$$\tau_f = \frac{\eta d_p}{\sigma} \tag{3.2.4}$$

where d_p is particle diameter and η is viscosity, which for silica displays Arrhenius-like behavior as a function of temperature (Frenkel, 1945). The property data of both titania and silica are shown in Table 3.2.1.

Table 3.2.1: Property data of titania and silica.

SiO_2	Surface tension	0.3 J m^{-2}	(Parikh, 1958)
	Viscosity	1.9 x 10^{-8} exp(6.1 x 10^4 / T) Pa s	(Hetherington et al., 1964)
TiO_2	Surface tension	0.5 J m^{-2}	(Astier et al., 1976)
	Diffusion coefficient	7.2 x 10^{-2} exp(-3.4 x 10^4 / T) cm^2 s^{-1}	(Anderson, 1967)
	Molecular volume for diffusion	1.6 x $10^{-23}$$cm^3$	(Bruce, 1965)

From the property data, following equations can be obtained to calculate the characteristic coalescence time of TiO_2 and SiO_2:

$$\tau_{f,TiO_2} = 1.5\times10^3 T d^3{}_p \exp(3.4\times10^4/T) \quad (3.2.5)$$

$$\tau_{f,SiO_2} = 6.3\times10^{-10} d_p \exp(6.1\times10^4/T) \quad (3.2.6)$$

Tables 3.2.2 and 3.2.3 show the computed characteristic sintering time of titania and silica with the various flame temperature and particle diameter from equations 3.2.5 and 3.2.6. The estimation shown in Table 3.2.3 is an upper bound coalescence time for SiO_2 likely even faster because of Na_2O salts which have been shown to lower SiO_2 viscosity (Hetherington et al., 1964). Figure 3.2.1 shows the time needed to heat up an individual titania particle up to 2100 K (melting temperature of TiO_2). In case of 10 nm silica particles, it takes 3 x 10^{-11} seconds to heat up the particle up to 2000 K (melting

temperature of SiO_2). The flame temperature and particle diameter in the tables and figure were chosen based on the experimental conditions in this thesis. The center temperatures of the TiO_2 and SiO_2 nanospheres were obtained by equation 3.2.7 and Heissler charts (Welty et al, 2001).

$$\frac{T-T_s}{T_0-T_s}=\frac{4}{\pi}\sum_{n=1}^{\infty}\frac{1}{n}\sin\left(\frac{n\pi}{D}r\right)e^{-(n\pi/2)^2 Fo} \tag{3.2.7}$$

where $Fo=\alpha t/(D/2)^2$, α is thermal diffusivity, T is center temperature of the particle, Ts is temperature of particle surface, T_0 is an initial particle temperature, n is relative position, r is distance from center to any point, t is time, and D is particle diameter.

From the comparison of the thermal relaxation time and the coalescence time with the residence time of particles in the flame and post-flame zone (see Table 3.1.2), it can be proved that enough time for the sintering of TiO_2 and SiO_2 nanoparticles was given in the experimental conditions of this thesis. Moreover, the difference between the residence time in the high temperature zone and the time required for the particle coalescence is several orders of magnitude. This suggests the residence time is sufficient for generating TiO_2/SiO_2 core-shell structure by sintering of particles in an atomized droplet.

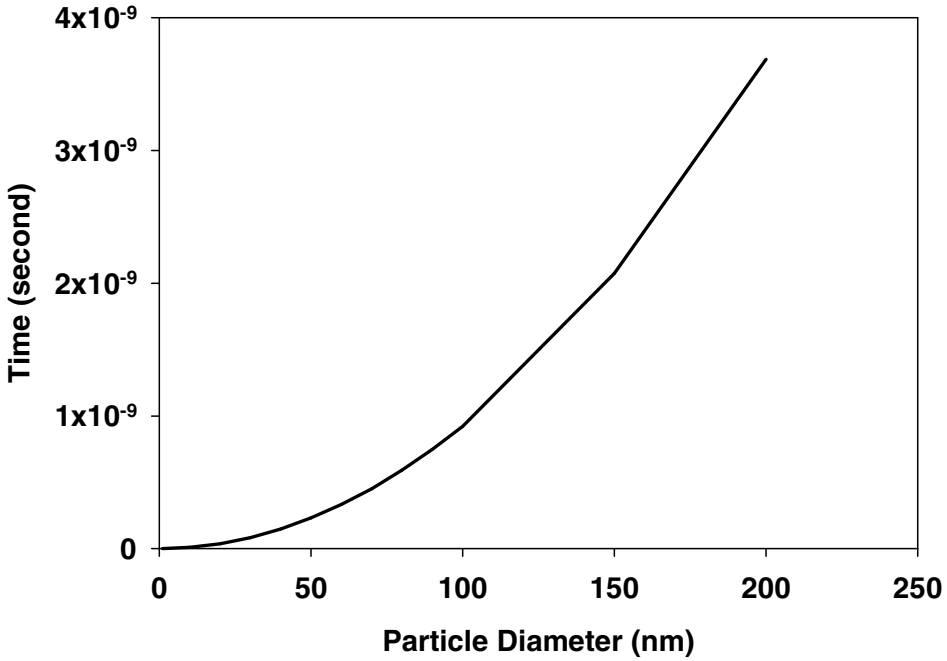

Figure 3.2.1: The time needed to heat up an individual TiO_2 particle from 298 K up to 2100 K when there is negligible surface resistance.

Table 3.2.2: The characteristic coalescence time of TiO_2 with respect to the adiabatic flame temperature and the particle diameter.

Particle diameter (nm)	Adiabatic flame temperature (K)				
	1800	2000	2200	2300	2400
	Characteristic coalescence time (second) of TiO_2				
10	4×10^{-10}	7×10^{-11}	2×10^{-11}	9×10^{-12}	5×10^{-12}
50	5×10^{-8}	9×10^{-9}	2×10^{-9}	1×10^{-9}	6×10^{-10}
100	4×10^{-7}	7×10^{-8}	2×10^{-8}	9×10^{-9}	5×10^{-9}
150	2×10^{-6}	2×10^{-7}	6×10^{-8}	3×10^{-8}	2×10^{-8}
200	4×10^{-6}	6×10^{-7}	1×10^{-7}	7×10^{-8}	4×10^{-8}

Table 3.2.3: The characteristic coalescence time of SiO_2 with respect to the adiabatic flame temperature and the particle diameter.

Particle diameter (nm)	Adiabatic flame temperature (K)		
	2200	2300	2400
	Characteristic coalescence time (second) of SiO_2		
10	3×10^{-5}	7×10^{-6}	2×10^{-6}

4. Results and Discussion

4.1 Flame Temperature Effect on TiO_2 Particle Size Modification

The effect of flame temperature on the particle size of TiO_2 nanoparticles was investigated prior to the silicon dioxide coating experiments. Table 2.2.1 shows experimental conditions of titania particle size modification experiments.

Figure 4.1.1 shows the TEM image and particle size distribution of initial titania nanoparticles. Three flame conditions were chosen for this experiment, with adiabatic flame temperatures of 1800 K, 2000 K, and 2400 K.

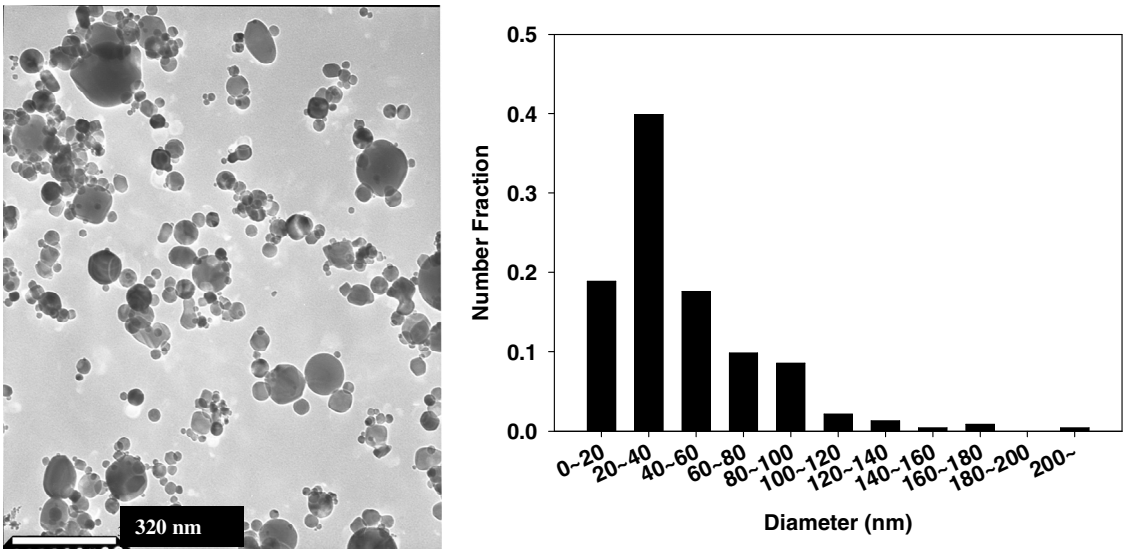

Figure 4.1.1: Transmission electron microscope image of initial titanium oxide nanoparticles and the particle size distribution.

Figures 4.1.2, 4.1.3, and 4.1.4 show the images of product titania nanoparticles and the particle size distributions. Both size distributions in the Figures 4.1.2 and 4.1.3 illustrate a decrease in the number of smallest particles (range of 0 to 20 nm) and an

increase in the number of the particles in the range of 40 nm to 60 nm compared with the initial size distribution of TiO_2 particles. Since the melting temperature of TiO_2 is 2100 K, size modification was not considerable when the flame temperature was under the melting temperature of titanium dioxide. Atomic diffusion, however, gives rise to size modification of titania nanoparticles at temperatures below the melting temperature. The size distribution in the Figure 4.1.4 shows significant particle size modification of TiO_2 nanoparticles because the temperature of premixed hydrogen/air flame was 2400 K, far above the melting temperature of titania particles.

Table 4.1.1 shows the number mean diameter of TiO_2 particles obtained from the measurements of particle diameters in the TEM images, from Figures 4.1.1 through 4.1.4. As mentioned above, at the adiabatic flame temperature of 1800 K and 2000 K, the change in particle diameter was little. At the adiabatic flame temperature of 2400 K, however, significant size modification was occurred.

Table 4.1.1: Number mean diameters of initial TiO_2 particles and product particles from the adiabatic flame temperature of 1800 K, 2000 K, and 2400 K.

TiO_2 conditions	Initial	Modified at T_{ad} = 1800 K	Modified at T_{ad} = 2000 K	Modified at T_{ad} = 2400 K
Particle diameter (nm)	44	53	50	96

From the size distribution of modified titania particles which was generated from the adiabatic temperature of 2400 K, mean particle size of 96 nm and particle volume of 4.7×10^{-22} m^{-3} were obtained. The theoretical calculation based on the droplet size of 1.05 μm, mean size of initial titania nanoparticle of 44 nm, and the solution condition showed

that, on average, each water droplet should contain 20 TiO_2 particles. The expected modified particle volume is 8.6 x 10^{-22} m^{-3}. The product particle volume was the same order of magnitude as the predicted volume and this verifies that all the components in the each atomized water droplet can be sintered together when the flame temperature is higher than the melting temperature of the components.

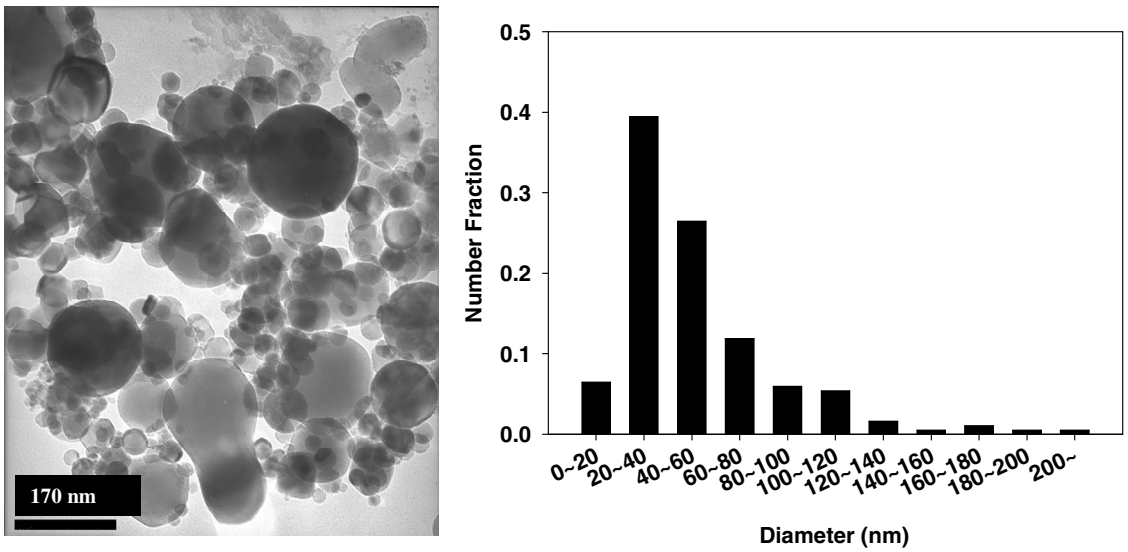

Figure 4.1.2: Transmission electron microscope image of size modified titanium oxide nanoparticles and the particle size distribution (adiabatic flame temperature of 1800 K).

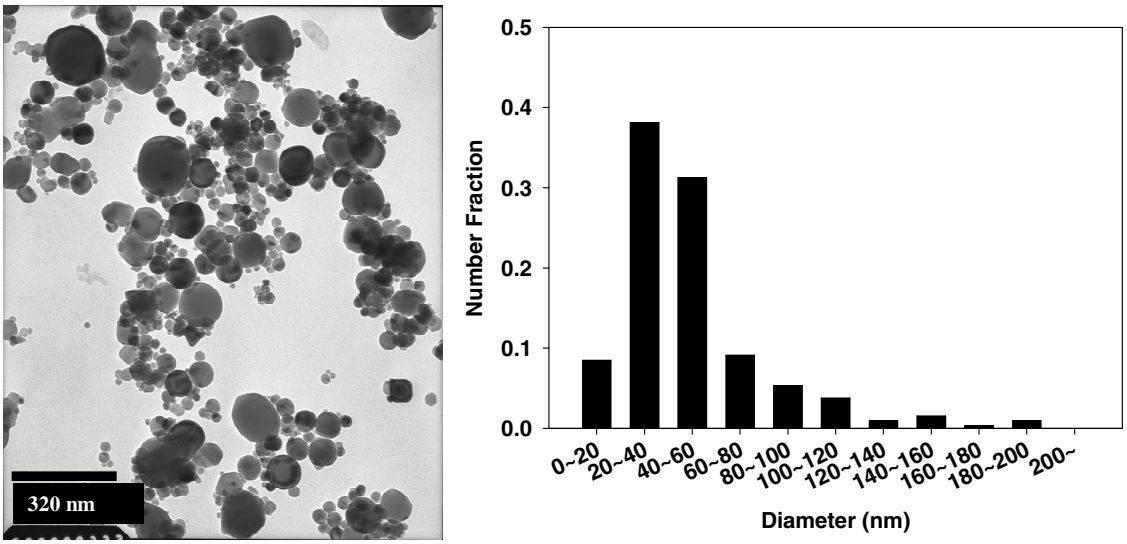

Figure 4.1.3: Transmission electron microscope image of size modified titanium oxide nanoparticles and the particle size distribution (adiabatic flame temperature of 2000 K).

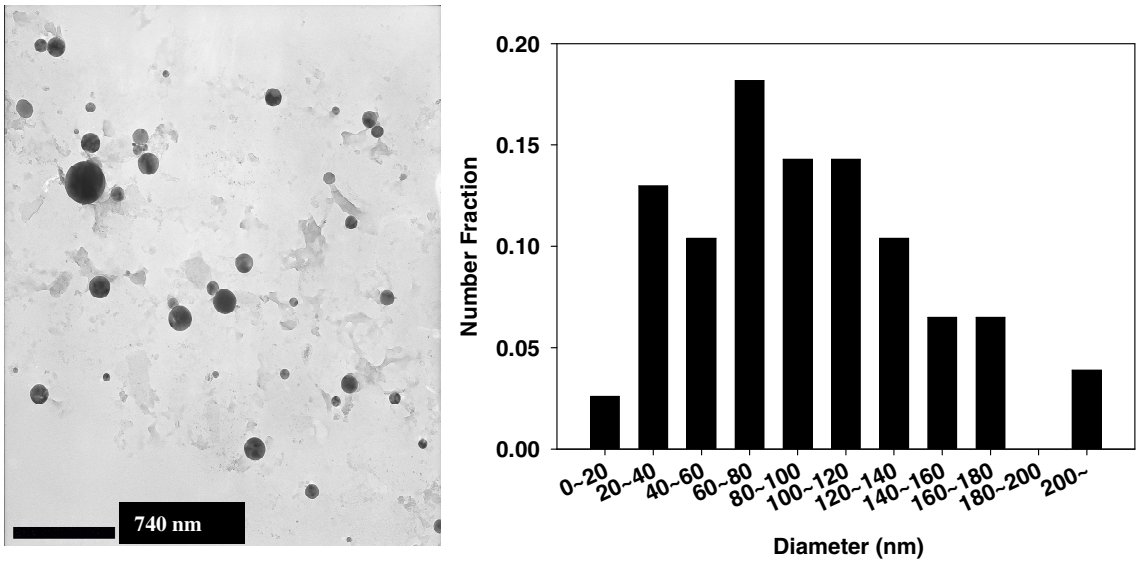

Figure 4.1.4: Transmission electron microscope image of size modified titanium oxide nanoparticles and the particle size distribution (adiabatic flame temperature of 2400 K).

4.2 Characterization of SiO_2 Coated TiO_2 Particles with HRTEM

SiO_2 Shell Volume

The product particles were characterized to determine morphology and shell volume by analyzing TEM images taken with a field emission transmission electron microscope (JEOL 2100F). If all the components of the droplet sinter together, the product particle volume is proportional to the mass loading in a droplet if the density of the particle remains constant. In this thesis, experiments were performed with this assumption. So, by varying the mass loadings of TiO_2 and SiO_2 in water droplet, it is possible to control the SiO_2 shell thickness.

Theoretical calculations were used to verify this assumption and the results are given in Figures 4.2.1 and 4.2.2. To calculate the total particle diameter and SiO_2 shell volume, droplet size distribution was obtained from the droplet size measurement experiment (see Appendix A). Then, from the known densities of TiO_2, SiO_2, and water in solutions, the total and the individual mass of titania and silica in one droplet can be obtained. By using the densities of the oxide particles, it is possible to estimate product titania and silica particle volume in the droplet. The total product particle diameter can be estimated from the total volume of the product particle.

It is hard to distinguish the three lines in the Figure 4.2.1 because the difference between the values of computed SiO_2 shell volume is small. So, Figure 4.2.2 is plotted additionally over a small range of particle diameter to distinguish the lines which are shown as one line in Figure 4.2.1.

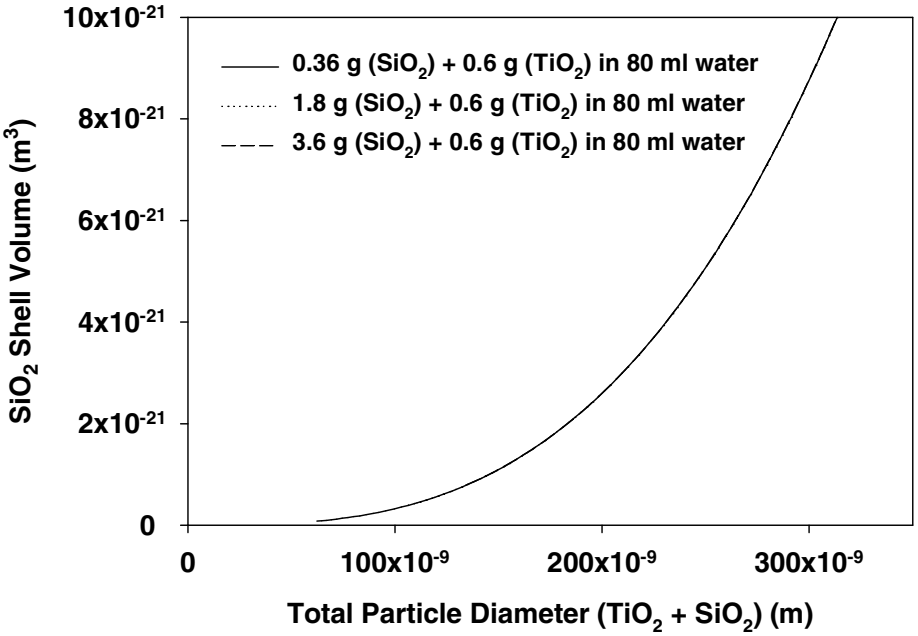

Figure 4.2.1: Plot of theoretical prediction of silica shell volume.

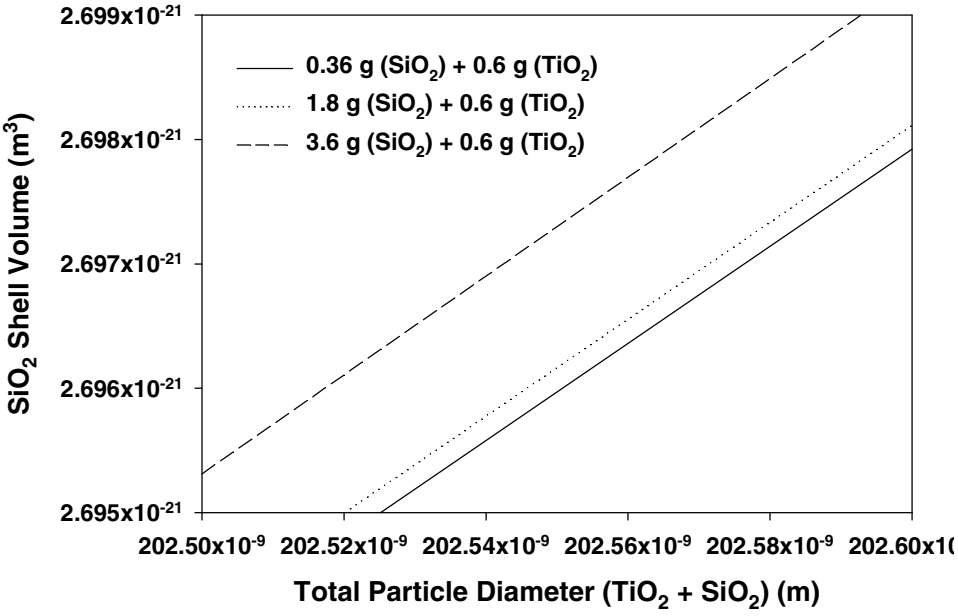

Figure 4.2.2: Enlargement of Figure 4.2.1 with total particle diameter from 202.5 nm to 202.6 nm and with SiO_2 shell volume from 2.695 x 10^{-21} m^3 to 2.699 x 10^{-21} m^3.

From Figures 4.2.3 through 4.2.5 show the comparison of predictions of shell volume versus particle diameter and results from TEM images. All the measurements in each plot are fitted by cubic regression. The results obtained from TEM images showed reasonable agreement with the predictions. There are two possible reasons why the experimental values of the shell volume are less than the predictions with respect to the same product particle diameter. The one reason is that the TiO_2 agglomerates are polydisperse, and difficult to mix well. Therefore droplets may contain more or less TiO_2 than the amount expected from the initial TiO_2/SiO_2 ratio. If the amount of TiO_2 is less than expected, it is difficult to see contrast in the TEM image and the core-shell particle may be mistaken for pure silica. If the amount of TiO_2 is greater than expected, the SiO_2 volume may be less than expected, assuming the mass loading is relatively constant from droplet to droplet. Another possible reason is that some Ti^{4+} may have diffused into the silica shell, creating an interface that is not sharp. Thus there may be some SiO_2 in the region considered to be the TiO_2 core.

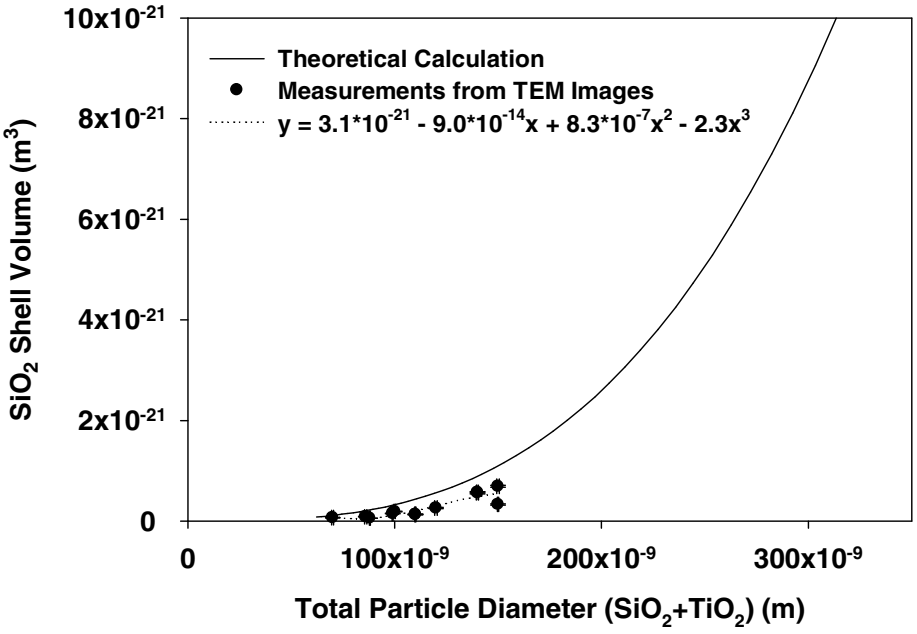

Figure 4.2.3: Comparison of computed values with the measurements from TEM analysis. Experimental condition of 0.36 g SiO_2 + 0.6 g TiO_2 in 80 ml deionized water. Error bars represent measurement uncertainty and in some cases the same size or smaller than data point markers.

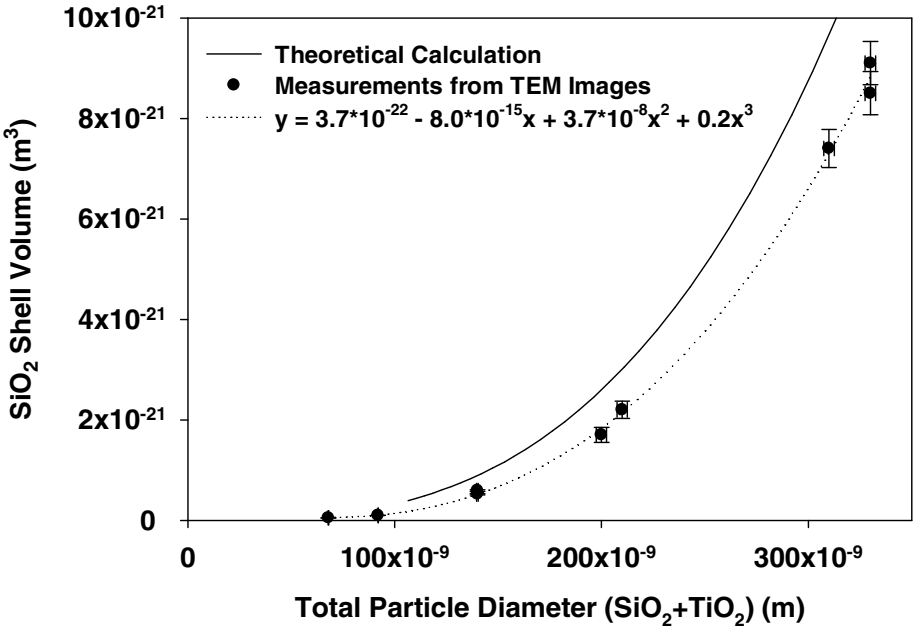

Figure 4.2.4: Comparison of computed values with the measurements from TEM analysis.

Experimental condition of 1.8 g SiO_2 + 0.6 g TiO_2 in 80 ml deionized water.

Same definition for error bars as in Figure 4.2.3.

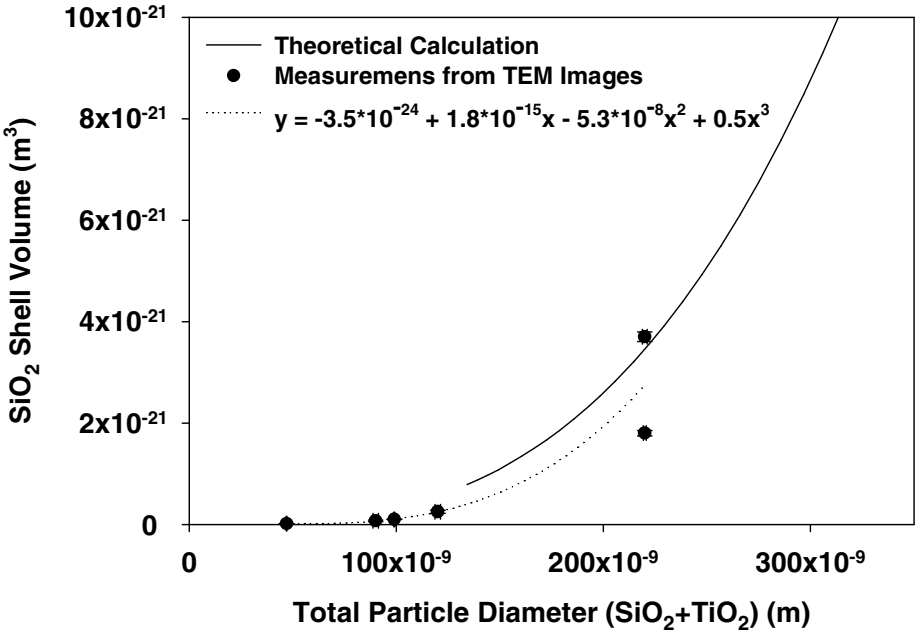

Figure 4.2.5: Comparison of computed values with the measurements from TEM analysis.

Experimental condition of 3.6 g SiO_2 + 0.6 g TiO_2 in 80 ml deionized water.

Same definition for error bars as in Figure 4.2.3.

Figure 4.2.6 compares the results from three different experimental conditions by fitting the results obtained from TEM images. It also shows reasonable agreement with the Figure 4.2.1 which predicts silica shell volume with respect to total product particle diameter.

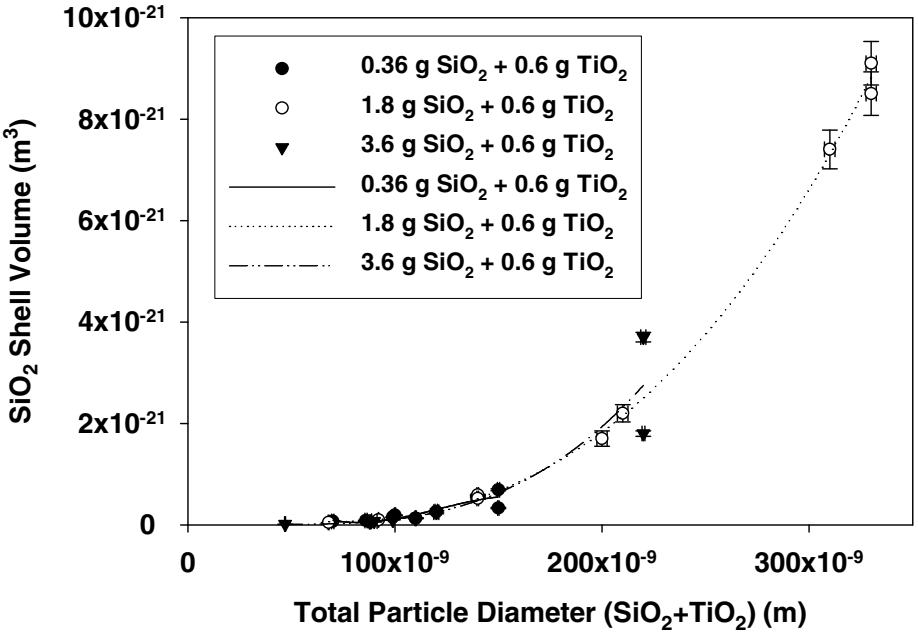

Figure 4.2.6: Comparison of results from three experimental conditions by fitting measurements obtained from TEM images.

Same definition for error bars as in Figure 4.2.3.

Particle Morphology

The main morphology observed in the product particles was (a) smooth SiO_2 coating on the sintered TiO_2 particles. Additionally, the morphologies of (b) two separate domains of TiO_2 and SiO_2 in a sphere particle, and (c) pure sintered TiO_2 and SiO_2 particles were observed as minor product particles Pure TiO_2 was rarely observed. Pure silica particles and separate TiO_2 and SiO_2 domain morphologies were each observed in approximately 10 % of the particles. These three main morphologies are believed to have originated from the arrangement of initial oxide particles in the water droplet (see Figure 1.1.1). When the oxides arrange in the form of A in Figure 1.1.1, the core-shell type of morphology will be manufactured. From the B and C arrangements, (b) and (c) types of morphology can be produced respectively. The tendency of interfacial energy reduction during the oxide particles coalescence also causes the formation of (a) and (b) types of product particles. One of the reasons why the (c) type of particles is observed is related to the degree of solution mixing. If the colloidal solution is not uniformly mixed, there are possibilities that some of the droplets include both TiO_2 and SiO_2 particles and some of the droplets only contain one kind of oxide particle, especially SiO_2. There were also peanut-shaped product particles which seemed to be formed by collision of sintered particles during the coalescence process.

Figure 4.2.7 shows the morphology of a TiO_2 and SiO_2 particle cluster from a dried water droplet collected right before the flame reactor and Figure 4.2.8 shows initial SiO_2 particles. Initial TiO_2 particles are shown in Figure 4.1.1. Figure 4.2.9 through 4.2.11 show the particle morphologies from the each experimental condition. From Figures 4.2.9, 4.2.10, and 4.2.11, smooth coatings of SiO_2 can be observed with the dark

TiO_2 core. The contrast in the images results from the difference in atomic number and crystallinity of TiO_2 and SiO_2. Diffraction of the incident electron beam at a crystalline area causes the area to look darker than an amorphous area in the TEM image. The orientation of the crystalline region with respect to the electron beam may also affect contrast (Eberhart, 1991).

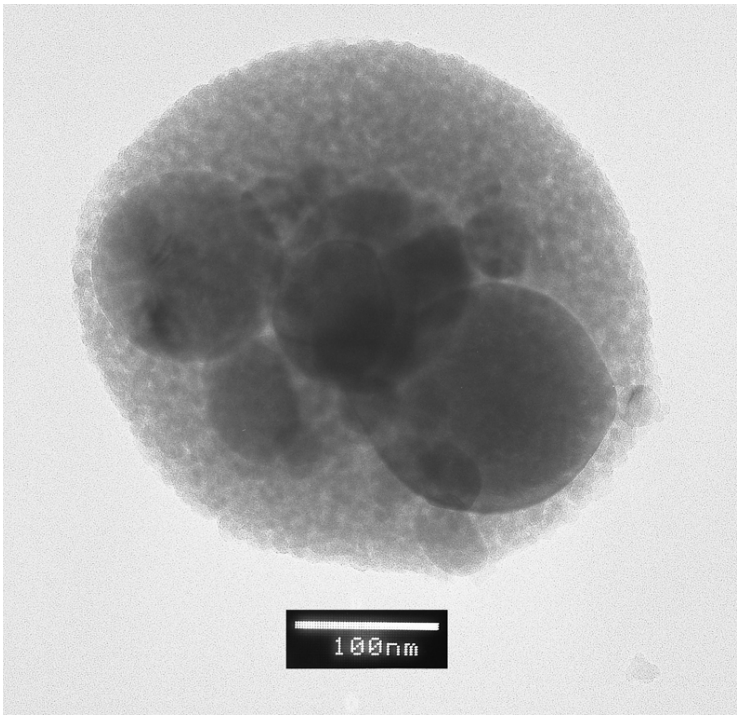

Figure 4.2.7: Morphology of TiO_2 and SiO_2 particle cluster from dried water droplet which is collected right before the flame reactor.

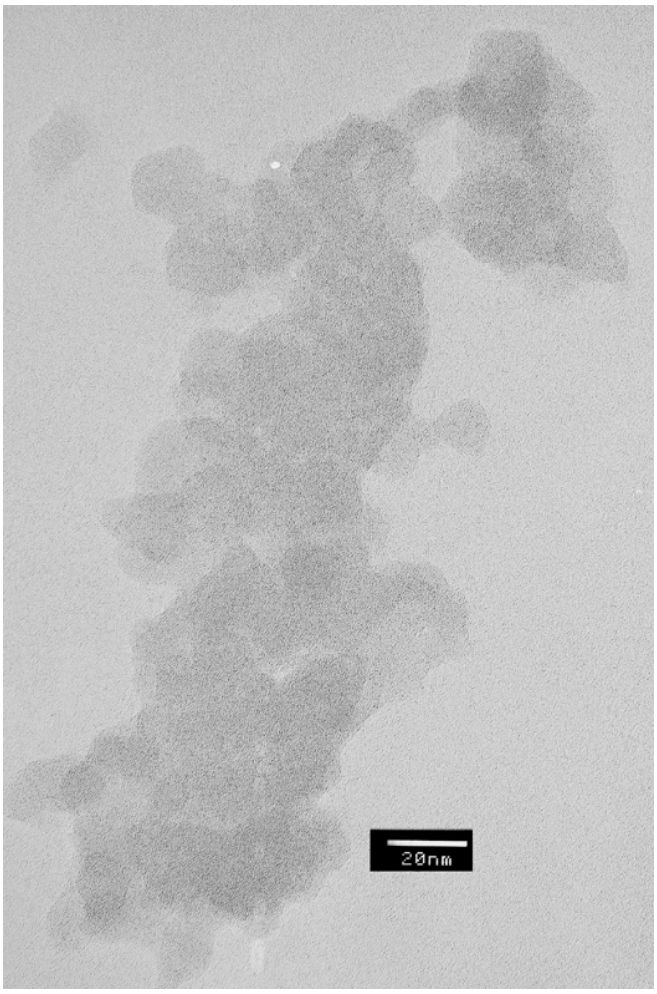

Figure 4.2.8: Initial SiO_2 particles.

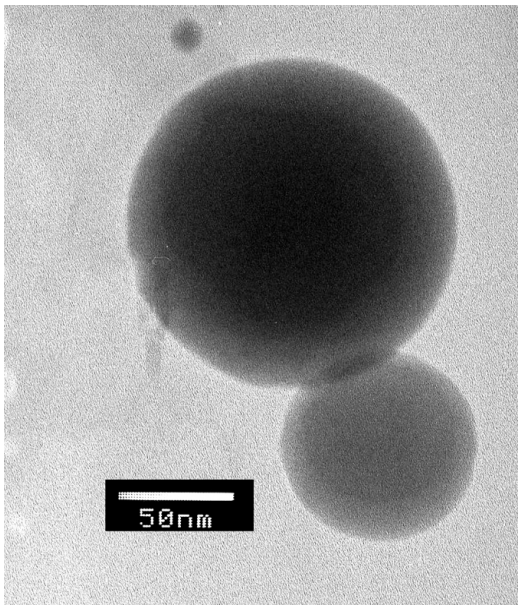

Figure 4.2.9: Product particles produced with the solution condition of 0.36 g SiO_2 + 0.6 g TiO_2 in 80 ml and an adiabatic flame temperature of 2300 K. Particles were collected at the height of 13 cm from the flame front.

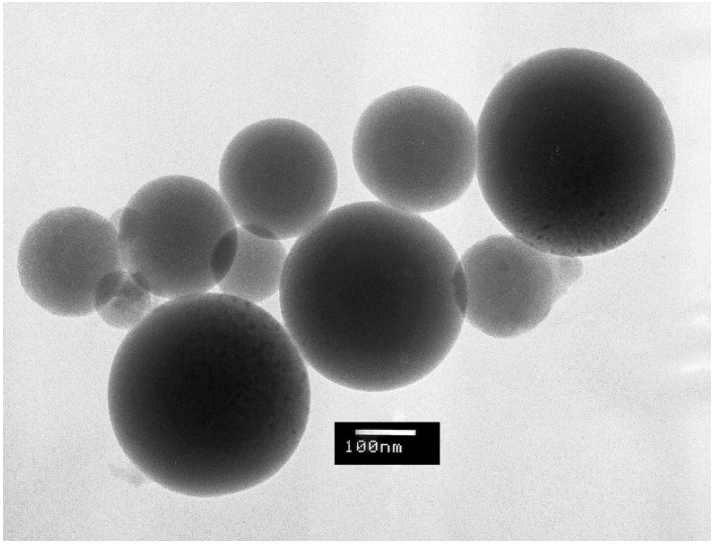

Figure 4.2.10: Product particles produced with the solution condition of 1.8 g SiO_2 + 0.6 g TiO_2 in 80 ml and an adiabatic flame temperature of 2300 K. Particles were collected at the height of 13 cm from the flame front.

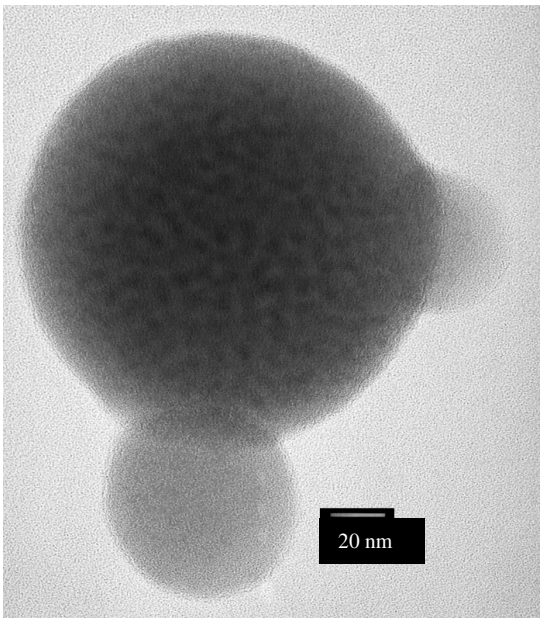

Figure 4.2.11: Product particles produced with the solution condition of 3.6 g SiO_2 + 0.6 g TiO_2 in 80 ml and an adiabatic flame temperature of 2300 K. Particles were collected at the height of 13 cm from the flame front.

Figure 4.2.12 shows the product particle of (b) type. The upper hemisphere of the particle is composed of amorphous silica, and the lower part of the sphere is composed of crystalline titania. The lattice fringes shown in the images verify this because these fringes give information about the crystal orientation on a very fine scale (Williams et al., 1996).

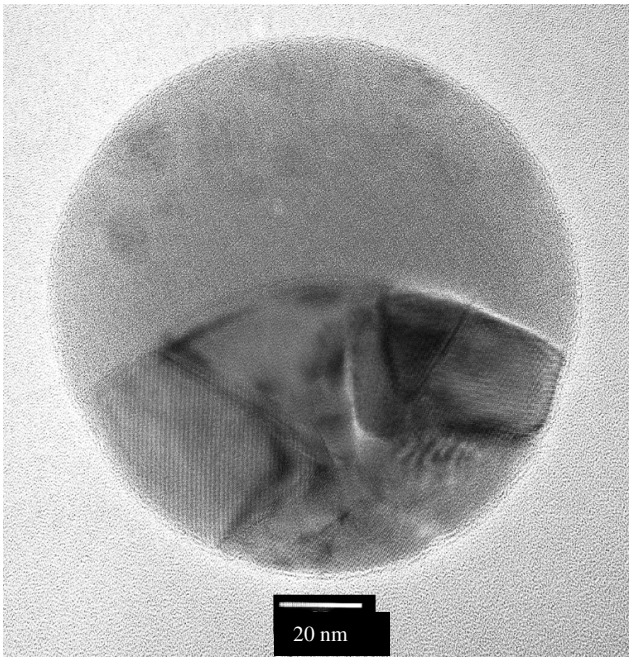

Figure 4.2.12: Product particle produced with the solution condition of 0.36 g SiO_2 + 0.6 g TiO_2 in 80 ml and an adiabatic flame temperature of 2300 K. Particles were collected at the height of 13 cm from the flame front.

5. Conclusion

A new approach for producing SiO_2 coated TiO_2 particles was presented in this thesis. Prior to the production of core-shell particles, size modification of titania experiments were performed. At the adiabatic flame temperatures of 1800 K and 2000 K, less than the melting temperature of titania, the degree of particle size modification was little. At the adiabatic flame temperature of 2400 K which is above the melting temperature of titania, however, considerable size modification of TiO_2 particles was observed.

The core-shell system of TiO_2 and SiO_2 was manufactured by a spray pyrolysis method, using agglomerated titania particles and colloidal silica particles as starting materials, in a high temperature hydrogen/air premixed flame. The flame conditions provided sufficient residence time for coalescence of the oxide particles within the flame and post-flame zone.

The SiO_2 shell volume versus product particle diameter was predicted from measurements of droplet diameters, obtained from an integrated system, the scanning mobility particle sizer (SMPS) (see Appendix A) and the concentration of the colloidal oxide solutions. The size measurements of product core-shell particles showed a reasonable agreement with the theoretical predictions. Differences may have resulted from inclusion of more or less TiO_2 particles in a droplet than the amount expected from the initial TiO_2/SiO_2 ratio, or diffusion of Ti^{4+} into the silica shell. The main morphology of the product particles was SiO_2 coated onto a TiO_2 core surface. The morphologies of either two separate regions composed of TiO_2 and SiO_2 in a spherical particle and pure sintered TiO_2 and SiO_2 particles were observed. The morphologies of product particles

were likely controlled by initial arrangement of starting oxides in the atomized droplets and particle collision during the sintering process.

This new method is very promising as a route for manufacture of core-shell particles, especially in the case of two oxide particles having different melting temperatures. Moreover, the coating layer produced by this method is very smooth and thickness can be controlled.

6. Recommendations for Future Work

Product Particle Size Control by Using Various Droplet Size

A homemade, collision type atomizer, which has volume average diameter of 1.05 μm, was used for the size modification experiments and coating experiments illustrated in this thesis. The result showed that the product particle diameters and volumes of shell reasonably agreed with theoretical calculations. This means product particle sizes can be predicted from the water droplet size distribution with known concentration of oxide particles and water in the solution. Thus, if other nebulizers which have different droplet sizes are used, and the loading and ratio of each component are varied, it should be possible to manufacture particles with a predictable core diameter and shell thickness.

Production of CeO_2 and Al_2O_3 Core-Shell System with Premixed Hydrogen/Oxygen Flame

The core-shell system synthesis method presented in this thesis is quite simple and can be applied to manufacture of another core-shell structure particles. Especially, by changing the oxidizer of hydrogen/air flame from air to oxygen, the application range of this method can be expanded to materials which have high melting temperatures because the hydrogen/oxygen flame can provide fairly high flame temperatures of up to 3400 K.

Production of CeO_2 and Al_2O_3 core-shell system is one of the examples where this method could be applied. Cerium oxide containing materials have been the focus of many investigations in recent years. Recently, the use of cerium oxide as an ultraviolet-shielding agent has been proposed (H. Isabelle, F. Serge, US patent 6 183 728 6). CeO_2, however, has high catalytic activity. It accelerates the decomposition of organic

substrates by oxidation (Cui et al., 2002). Surface coating of cerium oxide with zirconium oxide or aluminum oxide, can be one possible method to solve the problem.

CeO_2 has a high melting point of 2700 K and the melting temperature of Al_2O_3 is 2300 K. Hydrogen/oxygen flame can provide considerably high temperature and long residence time in the flame and post-flame zone. Both enable viscous flow coalescence and solid state diffusion during the sintering process of the particles.

Use of different sizes of SiO_2 particles

In this study, 10 nm SiO_2 particles were used as coating materials. When the method presented in this thesis is applied to producing of other core-shell particles, however, the size of 10 nm is not always available for other oxides used as coating materials. Thus, it is important to investigate the effect of initial particle size of coating material on the morphology and size of product particles even if the properties of the other oxides affect ones of product particles in different ways.

Appendices

Appendix A: Droplet Size Measurement

The size of nebulized water droplet was measured by using a dissolved NaCl solution with a known weight percentage of sodium chloride in the water. Sodium chloride ion solution was prepared by dissolving 1 g of crystalline sodium chloride (NaCl 99.99 %, Alfa Aesar) in 100 ml of deionized water. To estimate the volume mean size of the water droplets, an integrated system, the scanning mobility particle sizer (SMPS) was used. This system consists of electrostatic classifier (TSI 3080), condensation particle counter (TSI 3775), and aerosol instrument manager software (TSI). The aerosol instrument manager software enables near real time monitoring of particle size distributions, and can be used to obtain various kinds of particle size calculations: number particle size, volume particle size, and mass particle size. The sampling time was 120 seconds.

First, the sodium chloride solution was nebulized with the impact type atomizer by filtered compressed air and the air flow of 1 lpm (sheath flow was 10 lpm) was then transmitted to the electrostatic classifier at the same time. To completely remove water from the air flow, three diffusion dryers in series were used after the atomizer. Tygon tubing was used with all plastic connections to prevent loss of sodium chloride particles, because of the deposition of particles onto the tubing wall, during the transport.

The size distribution was measured 10 times. The first 5 samples were taken during the first 20 minutes and the interval between each sample was random. The estimated particle size was, however, decreasing with each subsequent sampling. Thus,

after waiting 10 minutes, another 5 samples were taken every 5th minute and the following results shown in Table 1 were obtained.

Table A.1: Estimated volume mean particle diameter of sodium chloride.

Sample number	Volume mean particle size (nm)
6	174.9
7	174
8	174.3
9	174.7
10	174.9

Figures A.1 and A.2 illustrate the obtained particle size distribution from the integrated system. Figure A.1 shows number distribution of NaCl particles with a geometric mean diameter of 84 nm and a geometric standard deviation of 1.6. Figure A.2 shows volume distribution of NaCl particles with a geometric mean diameter of 162nm and a geometric standard deviation of 1.5. The area in Figure A.2 is proportional to the mass of aerosol over a given size range.

If we assume the sodium chloride particles are perfect spheres, we can calculate the atomized water droplet size from the following equation.

$$\frac{m_{NaCl}}{m_{H_2O}} = \frac{\rho_{NaCl} \cdot \frac{\pi}{6} d^3{}_{NaCl}}{\rho_{H_2O} \cdot \frac{\pi}{6} (d^3{}_{H_2O} - d^3{}_{NaCl})} \qquad \text{(A.1)}$$

Here, d_{NaCl} and d_{H2O} are volume mean particle diameter. The estimated volume mean droplet size from the sample data and the equation (A.1) was 1.05 μm.

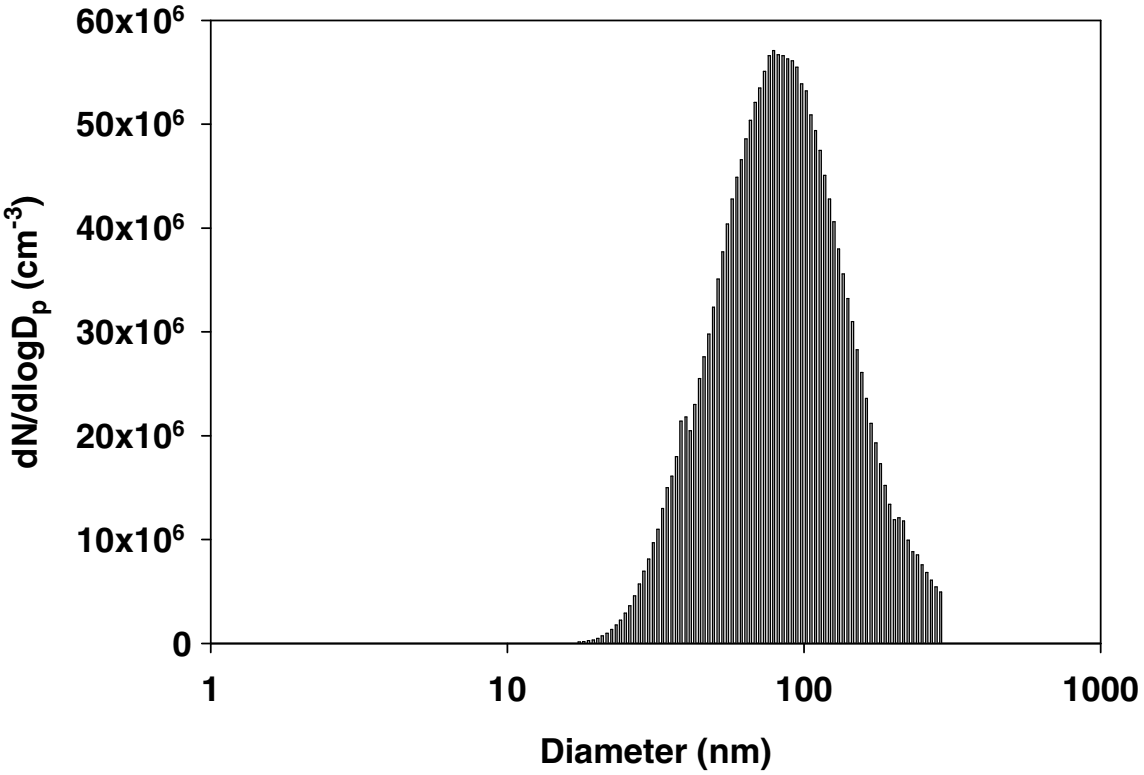

Figure A.1: Number size distribution of sodium chloride particles.

Particle diameter ranges from 7 nm to 289 nm with a geometric mean diameter of 84 nm and a geometric standard deviation of 1.6.

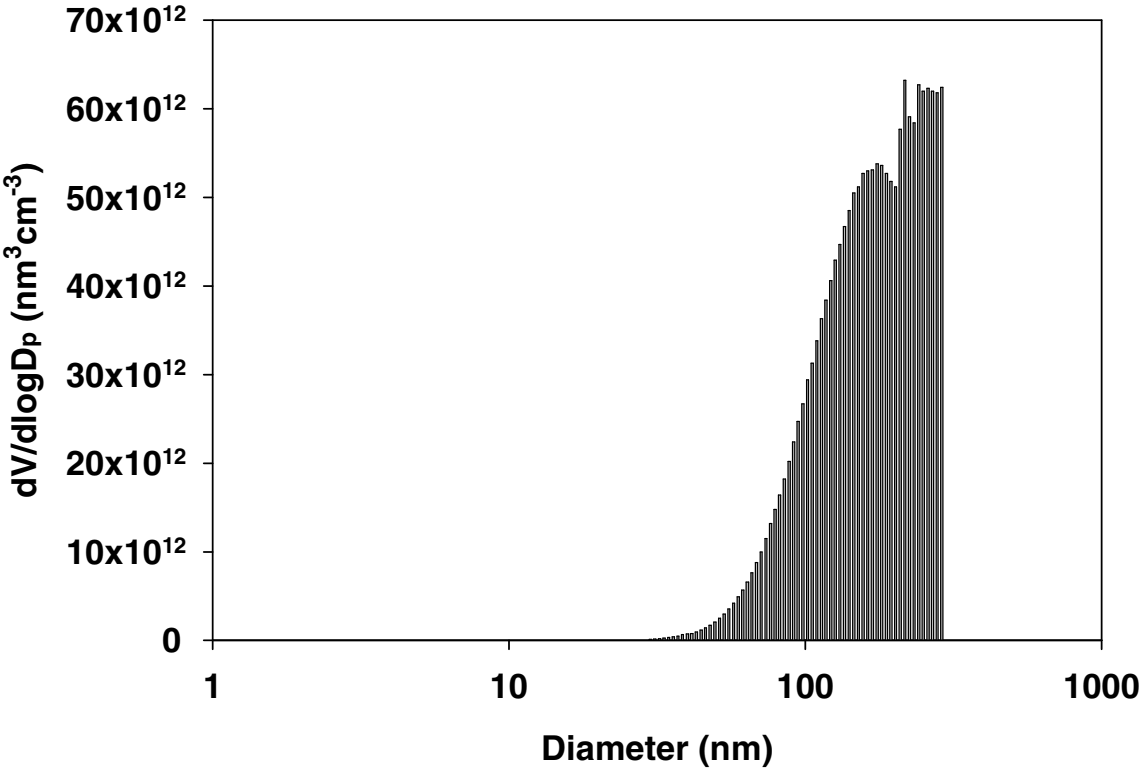

Figure A.2: Size distribution of sodium chloride particles weighted by particle volume. Particle diameter ranges from 7 nm to 289 nm with a geometric mean diameter of 162 nm and a geometric standard deviation of 1.5.

Appendix B: Temperature Profile

The temperature profile of the hydrogen/air flame was measured with a type S (platinum/10% rhodium-platinum, Omega) fine wire thermocouple which has length of 14.3 cm to the base and a ball diameter of 0.1 cm and a DPi32 (Omega) temperature meter. The temperature was measured along the centerline of the flame and corrected for radiation losses (Bradley et al., 1968). During the flame temperature measurement, the flame was generated only with pure air and hydrogen and no droplets were present because this can affect the flame temperature measurement by deposition of product particles onto the ball of thermocouple. The linear regression result of corrected temperature profile in Fig. B.1 gave a cooling rate of 100 Kcm^{-1}. The calculated adiabatic flame temperature was 2224 K and the maximum measured flame temperature was 2051 K.

The reasons of the discrepancy between the adiabatic flame temperature and the maximum measured temperature can be radiation losses, conduction losses in the thermocouple and conduction losses to the burner. The flow velocity near the tube wall is very low and is a major factor along with heat losses to the burner rim in stabilizing the flame at the top (Glassman, 1996).

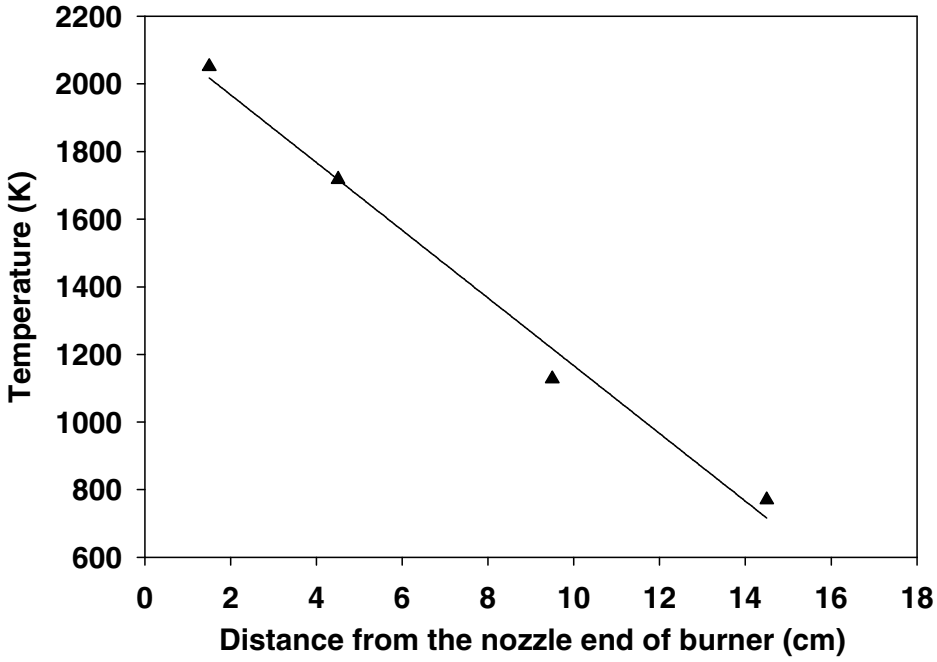

Figure B.1: Temperature profile along the centerline of the hydrogen/air flame at the experimental condition corresponding to an adiabatic flame temperature of 2224 K.

Appendix C: Standard Operation Procedure

1. weigh 0.6 g of TiO_2 powder and put it into a impact type atomizer
2. add exact amount of silica colloidal solution into the atomizer which is required to the specific experimental condition
3. add proper amount of water to make a desired concentrated solution
4. put a magnetic stir bar into the atomizer
5. atomize the solution for 30 min
6. record solution conditions
7. prepare thin aluminum foil, dimension of 13 cm x 13 cm, and clean it
8. wrap the aluminum foil around a cold finger
9. assemble the atomizer with experimental apparatus and put it onto a stirrer
10. start the stirrer
11. open the valve of filtered compressed air and adjust valves of pressure gauges and rotameters to get proper air flow rate (pure air: 22.5 L/min, droplet-laden air: 2.5 L/min)
12. wait for 3 ~ 5 minutes for the flow stabilization
13. open the valve of hydrogen cylinder and adjust the valves of the regulator and rotameter to get proper hydrogen flow rate (keep low the hydrogen flow rate when torching and increase the flow rate gradually to obtain target flame temperature)
14. wait for 3 ~ 5 minutes to stabilize all the flows
15. open the faucet of cooling water at the right side of the hood
16. torch with lighter

17. wait 3 ~ 5 minutes to obtain stable flame
18. locate the cold finger right above the center of flame and adjust height(14 cm ~ 16 cm from the burner) to prevent charring of the surface of aluminum foil (if the set height is lower than proper one, soot will be formed increasingly)
19. record start time, flow rates and pressure read of each stream
20. check the surface of the aluminum foil frequently (sometimes water droplet is formed by high cooling or soot is formed by height setting)
21. prepare TEM grids , deionized water and spatula to collect the product on to the TEM grids
22. after 2 hours, remove cold finger away from the flame
23. extinguish flame by fasten the valve which is located right before the burner
24. stop the flows of hydrogen and air by closing the valves right before the procedure 23
25. fasten the faucet of cooling water
26. turn off the stirrer
27. remove the aluminum foil from the cold finger carefully
28. unfold the foil
29. drop a little deionized water onto the one of the collecting side of the foil
30. scratch off the product particles with spatula
31. after finishing procedure 29, submerge the TEM grid in the water and collect the particles
32. collect remained colloidal dispersion in the vial and label it
33. repeat procedure from 28 through 32

34. remove the atomizer from the experimental apparatus

35. clean the atomizer and the magnetic stir bar with detergent using sonicator

36. keep the atomizer and the magnetic sir bar in a clean place

Appendix D: Index to TEM Grid Holder

Figure D.1: Index to TEM grid holder.

Figure number	Conditions	Grid location
4.1.1	Initial TiO_2	7A
4.2.8	Initial SiO_2	8Q
4.1.2	TiO_2 from 1800 K flame	5A, 5C
4.1.3	TiO_2 from 2000 K flame	7C, 7E
4.1.4	TiO_2 from 2400 K flame	8B, 8D
4.2.7	Custer of initial SiO_2 and TiO_2 from dried droplet	8S
4.2.9	2300 K flame 0.36 g SiO_2 + 0.6 g TiO_2 in 80 ml water	8K, 8M
4.2.10	2300 K flame 1.8 g SiO_2 + 0.6 g TiO_2 in 80 ml water	9L, 9N
4.2.11	2300 K flame 3.6 g SiO_2 + 0.6 g TiO_2 in 80 ml water	10K

References

Anderson, H. U. (1967). "Initial Sintering of Rutile". Journal of the American Ceramic Society. 50: 235.

Astier, M. and P. Vergnon (1976). "Determination of Diffusion-Coefficients from Sintering Data of Ultrafine Oxide Particles". Journal of Solid State Chemistry. 19: 67-73.

Bradley, D. and K. J. Matthews (1968). "Measurement of High Gas Temperatures with Fine Wire Thermocouples". Journal of Mechanical Engineering Science. 10: 299-305.

Brodkey, R. S. and American Institute of Chemical Engineers. (1975). "Turbulence in Mixing Operations: Theory and Application to Mixing and Reaction". New York, Academic Press.

Bruce, R. H. (1965). "In Science of Ceramics, Vol.2 (Edited by Steward, G.H.)". New York, Academic Press.

Carp, O., C. L. Huisman and A. Reller (2004). "Photoinduced Reactivity of Titanium Dioxide". Progress in Solid State Chemistry. 32: 33-177.

Cui, H. T., G. Y. Hong, X. Y. Wu and Y. J. Hong (2002). "Silicon Dioxide Coating of CeO_2 Nanoparticles by Solid State Reaction at Room Temperature". Materials Research Bulletin. 37: 2155-2163.

DiPasquale, G., A. Pollicino, A. Recca, F. A. Bottino and M. Sandri (1996). "Leucopur EGM Influence on the Surface Photooxidation of Poly (Ethylene Terephthalate) and Poly (Vinyl Chloride)". Polymer. 37: 703-705.

Eberhart, J. P. (1991). "Structural and Chemical Analysis of Materials". New York, Wiley.

Fitzwater, S. and J. W. Hook (1985). "Dependent Scattering-Theory - a New Approach to Predicting Scattering in Paints". Journal of Coatings Technology. 57: 39-47.

Frenkel, J. (1945). "Viscous Flow of Crystalline Bodies under the Action of Surface Tension". Journal of Physics. 9: 385.

Friedlander, S. K. and M. K. Wu (1994). "Linear Rate Law for the Decay of the Excess Surface-Area of a Coalescing Solid Particle". Physical Review B. 49: 3622-3624.

Fujishima, A., T. N. Rao and D. A. Tryk (2000). "TiO_2 Photocatalysts and Diamond Electrodes". Electrochimica Acta. 45: 4683-4690.

Glassman, I. (1996). "Combustion". San Diego, Calif., Academic Press.

Gratzel, M. (2001). "Photoelectrochemical Cells". Nature. 414: 338-344.

Hetherington, G., K. H. Jack and J. C. Kennedy (1964). "The Viscosity of Vitreous Silica". Physics and Chemistry of Glasses. 5: 130-136.

Hollande, S. and J. L. Laurent (1997). "Study of Discolouring Change in PVC, Plasticizer and Plasticized PVC Films". Polymer Degradation and Stability. 55: 141-145.

Iler, R. K. (1959). "Product Comprising a Skin of Dense, Hydrated Amorphous Silica Bound Upon a Core of Another Solid Material and Process of Making Same." U.S. Patent: No. 2 885 366.

Kaempf, G., Papenrot.W and R. Holm (1974). "Degradation Processes in TiO_2-Pigmented Paint Films on Exposure to Weathering". Journal of Paint Technology. 46: 56-63.

Kinniard, S. P. and A. Campeotto (2003). "Method for Manufacturing High Opacity, Durable Pigments." U.S. Patent: No. 6 528 568 B522.

Koch, W. and S. K. Friedlander (1990). "The Effect of Particle Coalescence on the Surface-Area of a Coagulating Aerosol". Journal of Colloid and Interface Science. 140: 419-427.

Kubota, Y., C. Niwa, T. Ohnuma, Y. Ohko, T. Tatsuma, T. Mori and A. Fujishima (2001). "Protective Effect of TiO_2 Particles on UV Light Induced Pyrimidine Dimer Formation". Journal of Photochemistry and Photobiology a-Chemistry. 141: 225-230.

Murphy, J. (1996). "The Additives for Plastics Handbook". Kidlington, Oxford, UK, Elsevier Advanced Technology.

Nussbaumer, R. J., W. R. Caseri, P. Smith and T. Tervoort (2003). "Polymer-TiO_2 Nanocomposites: A Route Towards Visually Transparent Broadband UV Filters and High Refractive Index Materials". Macromolecular Materials and Engineering. 288: 44-49.

Parikh, N. M. (1958). "Effect of Atmosphere on Surface Tension of Glass". Journal of the American Ceramic Society. 41: 18-22.

Powell, Q. H., T. T. Kodas and B. M. Anderson (1996). "Coating of TiO_2 Particles by Chemical Vapor Deposition of SiO_2". Chemical Vapor Deposition. 2: 179-181.

Santacesaria, E., S. Carra, R. C. Pace and C. Scotti (1982a). "Vapor-Phase Treatment of Titanium-Dioxide with Metal Chlorides.1. The Reactions of Coating Performed by Al_2Cl_6, $SiCl_4$, and $ZrCl_4$ in the Vapor-Phase". Industrial & Engineering Chemistry Product Research and Development. 21: 496-500.

Santacesaria, E., S. Carra, R. C. Pace and C. Scotti (1982b). "Vapor-Phase Treatment of Titanium-Dioxide with Metal Chlorides.2. Kinetics of the Reaction between Titanium-Dioxide and Aluminum-Chloride". Industrial & Engineering Chemistry Product Research and Development. 21: 501-504.

Thiele, E. S. and R. H. French (1998). "Computation of Light Scattering by Anisotropic Spheres of Rutile Titania". Advanced Materials. 10: 1271-1276.

Volz, H. G., G. Kaempf, H. G. Fitzky and A. Klaeren (1980). "Chemical Nature of Chalking in the Presence of TiO_2 Pigments". Abstracts of Papers of the American Chemical Society. 179: 103.

Welty, J. R., C. E. Wicks, R. E. Wilson, G. Rorrer (2001). "Fundamentals of Momentum, Heat, and Mass Transfer". New York, John Wiley.

Werner, A. J. (1969). "Titanium Dioxide Pigment Coated with Silica and Alimina". U.S. Patent: No. 3 437 502.

Williams, D. B. and C. B. Carter (1996). "Transmission Electron Microscopy". New York, Plenum Press.

Winkler, J. (2002). "Nano-Scaled Titanium Dioxide - Properties and Use in Coatings with Special Functionality". Macromolecular Symposia. 187: 317-323.

Wu, M. K., R. S. Windeler, C. K. R. Steiner, T. Bors and S. K. Friedlander (1993). "Controlled Synthesis of Nanosized Particles by Aerosol Processes". Aerosol Science and Technology. 19: 527-548.